

Removing proteins or bacteria on a tilted surface using air bubbles

Alireza Hooshanginejad,^{1,2} Timothy Sheppard,¹ Purui Xu,³ Janeth Manyalla,¹ John Jaicks,¹ Ehsan Esmaili,⁴ and Sunghwan Jung^{1,*}

¹*Department of Biological and Environmental Engineering,
Cornell University, Ithaca, New York, USA.*

²*School of Engineering, Brown University, Providence, Rhode Island, USA.*

³*Department of Biomedical Engineering,
Cornell University, Ithaca, NY, USA.*

⁴*Department of Mechanical Engineering,
Purdue University, West Lafayette, Indiana, USA.*

(Dated: June 8, 2022)

Abstract

Cleaning surfaces with bubbles has been a topic of discussion in recent years due to the growing interest in sustainable methods for cleaning. Specifically, a method of using air bubbles to sanitize agricultural produce has been proposed as an eco-friendly alternative to current methods. In this study, we conduct experiments to test the cleaning efficacy at different angles of inclination of a contaminated surface. We use two different types of surface coated with either a protein solution or a bacterial biofilm. Our experimental results indicate that bubbles exhibit the best cleaning efficacy at the surface angle of $\theta \approx 20^\circ$ for polydisperse bubbles in the range of 0.3-2 mm and with an average radius of 0.6 mm in radius. To gain a better understanding of the underlying mechanism, we perform a numerical analysis of a single air bubble impacting surfaces with different angles. Our numerical and theoretical results show that the shear stress, which is proportional to the sliding speed but inversely proportional to the thickness of the film, results in the maximum shear force occurring at $\theta \approx 22^\circ \approx \pi/8$ which agrees well with the experiments.

* sunnyjsh@cornell.edu

I. INTRODUCTION

Multiphase flows have been used for the removal of micrometer-scale contaminants from surfaces for decades [1–3]. Specifically, air bubbles are proposed as a sustainable cleaning method for wastewater treatments [4–6], or preventing biofouling [7, 8]. Recently, agricultural produce such as fruits and vegetables has been cleaned with the insertion of air bubbles [9–11]. Developing such environmentally benign methods for sanitizing agricultural produce is important, as pathogens in fresh produce are recognized as the primary cause of foodborne diseases in millions of people each year [12–14]. From a practical point of view, numerical analysis of a bubble impacting and sliding on a tilted surface has shown that the maximum shear stress exerted on the surface is sufficient for removing different types of bacteria from the surface [11].

Bubble dynamics has been studied extensively in both a freely rising bubble [15–19] and a bubble interacting with either horizontal [20–25] or vertical [26–29] solid surfaces. However, only a few studies have investigated the dynamics of bubbles along a tilted solid surface [30, 31, 33–36]. Specifically, by incorporating lubrication approximation the thin film flow between the sliding bubble and the surface can be modeled [11, 33]. Then the shear stress can be quantified on the surface, which is the key in characterizing the cleaning effect of sliding bubbles. Although shear stress was recently calculated for varying surface angles [11], no experiments have yet verified the cleaning effect of air bubbles on tilted surfaces. In addition, while the maximum shear stress on the surface has been reported for different inclination angles [11], the average shear stress has not been studied for practical applications and comparison with potential experiments.

In this study, we perform experiments to use bubbles of millimetric scale and clean surfaces coated with either protein or bacterial coatings at different tilting angles of the surface. Our results show that there exists a critical angle for maximum cleaning effect. In addition, we perform numerical calculations of an air bubble impacting and sliding over the tilted surface incorporating the recent model on bubble dynamics near a tilted wall [11]. The manuscript is organized as follows. In section II, we discuss experimental methods including the coating procedure in section II A and the cleaning experiments in section II B, and numerical methods in section II C. We then present and discuss our experimental and computational results in section III. Finally, in section IV we summarize our findings and

discuss future studies.

II. MATERIALS AND METHODS

A. Coating Preparation

1. Protein Dirt Preparation

A protein dirt/soil solution is synthesized for glass slide coating. We first incorporate 100 g of 2% fat milk and 30 g of sifted wheat flour in a small pot with an immersion blender until the mixture reaches 115 °C, and a paste-like solid is formed. This mixture is then left to cool to 30 °C, wherein afterwards it is combined with another 120 g of milk and is blended again until a uniform solution remains after 10 minutes. Next, 6 g of Nigrosin dye is gently stirred in with a wooden tongue depressor until fully combined. Once completed, the mixture is sifted twice, first through a 500-600 μm mesh, then again through a 100-150 μm mesh. The resulting mixture is then ready to be used for coating.

2. Spin Coating of Protein Dirt

On the same day as protein preparation, glass microscope slides of 76.2 mm \times 25.4 mm \times 1.1 mm are cleaned and coated with the protein solution using a custom-designed spin coater. More information about making the spin coater including 3D printing designs can be found in [37]. To coat the slides, we first secure the slide tightly to the spin-coater plate with opposing metal bolts. Next, a 0.5 mL protein drop is gently deposited onto the middle of the slide and spinned for 10 seconds at a rate of $\Omega \sim 1100 - 1200$ rotations per minute (RPM). These coated slides are left to dry for 15 minutes inside a fume hood, then proceeded by a second coating of the same procedure. This second coating creates a more opaque surface which proved to be more effective in characterizing the cleaning effect of our tests. After the second coating, the slides are stored in a cool, dry place. In the current study, all slides are tested after drying for 2 full days. We note that the effect of the drying time was investigated in previous studies showing a decaying cleaning effect as the coating dries for longer periods [37].

3. Bacterial Coating Preparation

To test the bubble-cleaning effect with live organisms, we also prepare glass slides coated with *E. coli*. For better visualization, we introduce the green fluorescent protein (GFP) gene into *E. coli* (MM294 strain, Carolina Biological Supply Co.) with the heat-shock plasmid transformation method. Using a disposable sterile pipette, we add 250 μL of 50 mM CaCl_2 solution to a sterile micro-tube. Then we use a sterile inoculation loop to transfer 5 *E. coli* colonies from the source media to the tube, and immerse the loop tip into the CaCl_2 solution and vigorously span the loop to disperse the entire mass into the CaCl_2 solution. The tube is then placed in an ice bath. Next, we transfer 10 μL of 0.01 $\mu\text{g}/\mu\text{L}$ pGREEN (4528 bp) directly into the tube using a sterile pipette, and gently mix the solution with the pipette. The tube is incubated in an ice bath for 10 minutes. After that, we take the tube to the 42°C water bath, and hold the tube under water for 45 seconds to give the bacteria colony a heat shock, and immediately return the tube to ice. After 2 minutes, we add 250 μL of recovery Luria broth (LB) to the tube. We gently mix the solution, and incubate the tube at room temperature for 10 minutes. We label 1 LB agar plate and 1 LB/Ampicillin+GFP agar plate. The Ampicillin plate is critical for selecting the GFP transformed bacteria colonies, and is made with 100 μL of 10 mg/mL Ampicillin solution and 20 mL agar media. Using a sterile pipette, we transfer 50 μL of bacteria suspension from the tube to each plate and spread the bacteria. The plates are rested for 10 minutes, then sealed and incubated at 37°C upside down. After 24 hours of incubation, the GFP transformed colonies start to appear on the LB/Ampicillin+GFP plate. Using a sterile inoculation loop, we transfer the GFP transformed colonies to the LB broth and make a GFP *E. coli* suspension.

Next, in an aseptic experimental environment, we juxtapose four identical sterile glass slides inside a sterile Petri dish (140 mm diameter). We then add 33 mL of liquid LB agar media into the Petri dish to fully cover the glass slides by agar media. We let the agar cool down and solidify. The resulting thickness of the agar on each slide is 1 mm. We use a sterile pipette and transfer 25 μL of living *E. coli* suspension to the middle of the agar plate. We then roll sterile glass beads on the plate to evenly distribute the bacteria. Afterwards, the Petri dish is sealed with parafilm, and is rested for 10 minutes to let the agar plate absorb the bacteria suspension. Finally, the Petri dish is incubated at 37°C with the agar side on top for 72 hours. After the incubation, we gently cut the slides with the bacteria-agar layer

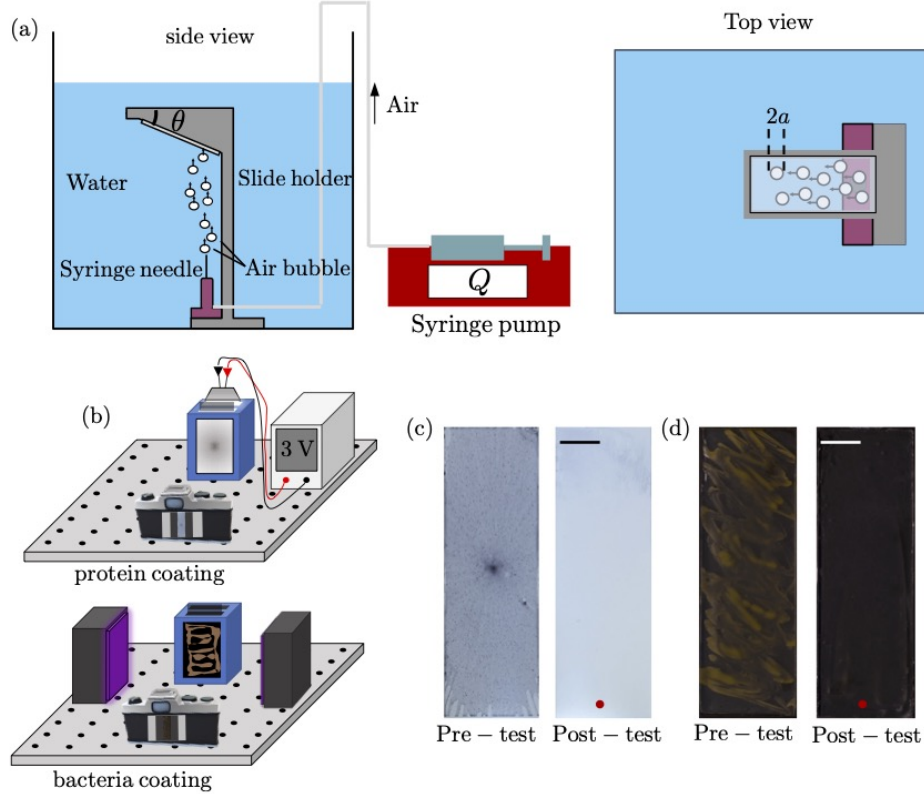


FIG. 1. (a) side-view and top-view schematics of the experiments. (b) Schematics of the slide imaging setup. (c) Pre-test and post-test images of a protein-coated slide for $\theta = 20^\circ$ and 6 minutes of bubble testing. (d) Pre-test and post-test images of a biofilm coated slide for $\theta = 20^\circ$ and 6 minutes of testing. The red dots in the post-test images show the location of the bubble releaser. on the top to use for the experiments.

B. Bubble Cleaning Experiment

A 20 L tank is first filled with room temperature deionized water. Within it, a 3D printed slide-carrying tower holds coated slides at an angle, θ , with regards to the bottom of the tank as shown in Fig. 1(a). At the base of this slide carrier, a 25 gauge syringe needle is placed 5 mm from the slide edge at a constant height of 11 cm from the surface. A 3D printed needle holder connects the syringe needle to an external syringe pump. Figure 1(a) shows the schematics for the side view and top view of the experiments.

Slides coated with proteins are imaged before and after each cleaning test utilizing a 3D printed LED slide stand fixed to an optical breadboard as illustrated in Fig. 1(b). The

LED is maintained at 3V using a DC power supplier. The LED is replaced with a uniform black-painted background illuminated by a set of UV lights for the bacteria-coated slides. A digital camera (Nikon 7500) is fixed to the board 1.5 ft away from the slide with a 105 mm macro lens. The system is utilized in a dark room. Slide images from before and after the tests are then analyzed by performing image processing. We note that all the post-test images were taken after one hour of drying in room temperature. Figures 1(c) and 1(d) show sample pre-test and post-test images with protein coating and bacteria coating, respectively. We note that for protein coatings, there is always a darker spot appearing in the center of the slide indicative of a thicker coating layer, while some areas near the edges are thinner (see Fig. 1(c)). However, since all slides are coated with the same method and include these features, the effect of such spots on the average cleaning results is negligible. On the contrary, surfaces coated with bacteria indicate more variations in the thickness of the biofilm, as shown in the pretest image of Fig. 1(d). We discuss the effect of such randomness in biofilm thickness on the cleaning results in section IV. To characterize the efficacy of bubble cleaning, the intensity matrix of the pre-test, post-test, and clean-slide images are converted to grayscale matrices of I_1 , I_2 , and I_0 , respectively. Hence, we define the total cleaning efficacy as $\lambda^t = (I_2 - I_1)/(I_1 - I_0)$. Therefore, as λ^t approaches 1, all coated contaminants are removed from the surface. To isolate the role of bubbles in cleaning, we run a series of control experiments with the same θ and T for each case where no bubbles are injected. We define the cleaning efficacy of the control experiments without bubbles in a similar way and denote it by λ^c . Then, we define the efficacy of cleaning bubbles as $\lambda = \lambda^t - \lambda^c$. It is noteworthy that λ^c for all cases is quite small compared to λ^t and does not change the trend between λ^t and λ significantly.

C. Numerical Methods

To gain a more fundamental understanding of λ , we implement a numerical model that includes all forces that contribute to the dynamics of a bubble impacting a tilted surface: the buoyancy force, the drag force, the lift force, the added mass force, and the thin film force. We expect the liquid film thickness to be on the order of micrometers and a stable liquid film force remains significant as the bubble moves near the tilted wall [11, 20]. This model has previously been discussed and studied for a similar condition where the bubble

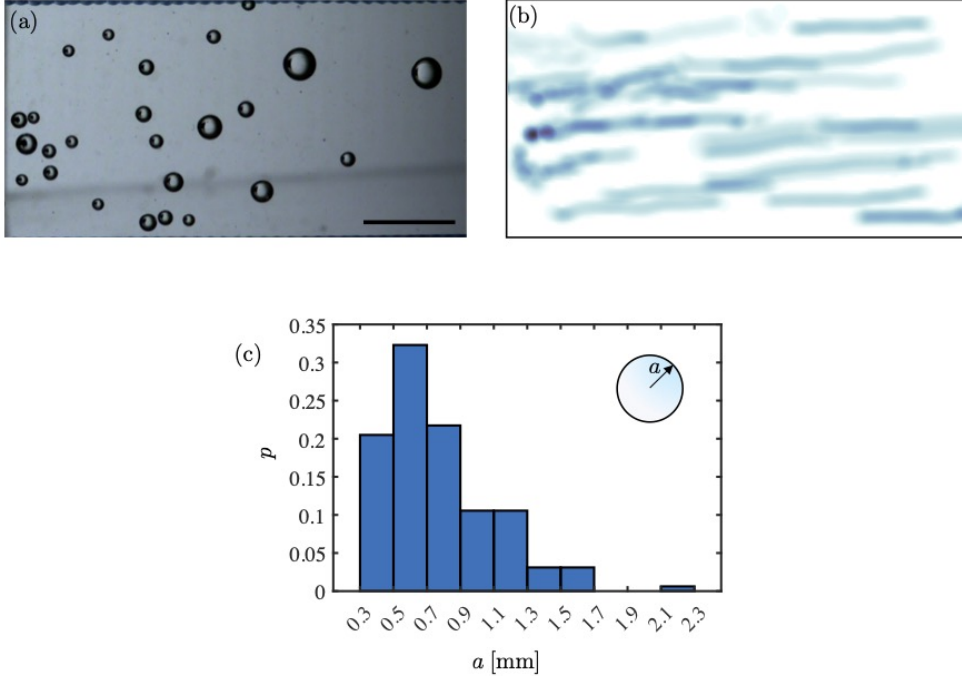


FIG. 2. (a) a snapshot of bubbles moving along a clean surface with $\theta = 10^\circ$. (b) trajectory of air bubbles for 0.4 seconds presented using an arbitrary color with a Gaussian blurring method at bubble centers. The Gaussian distribution has a root mean square width equal to a bubble radius. (c) Histogram of bubbles radius, a , for 5 different tests and approximately 200 bubbles.

impacts and slides over a tilted wall [11]. Hence, we only summarize the main features of the model herein and refer to [11] for further details. We note that in this study we focus on features of bubble dynamics that are different from previous work [11] to rationalize our current experimental results.

Figure 3 shows the schematic of a bubble impacting a tilted surface to introduce the notations used in our model. Both XYZ and xyz coordinates denote the axial direction, the transverse direction, and the direction normal to the surface, respectively. The XYZ origin is located on the first impact point, while the xyz origin is the bubble's centroid projected onto the surface which moves with the bubble. The bubble's centroid distance normal to the surface is denoted by H while it moves with velocities U , and V , along X and Y , respectively. In addition, the thin film thickness and the thin film pressure are denoted by $h(x, z, t)$ and $P(x, z, t)$, respectively. Hence, the force balance in X and Y yields as [11]

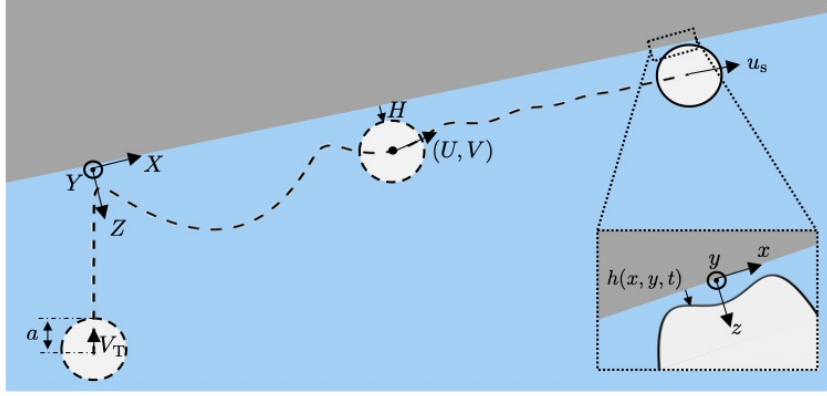


FIG. 3. Schematics of a bubble impacting a tilted surface from the bouncing to the sliding regime.

$$\rho\Omega \left[C_m^{\parallel} \frac{dU}{dt} - \frac{dC_m^{\parallel}}{dH} VU \right] = \rho g\Omega \sin(\theta) - \frac{\pi}{4} C_D^{\parallel} \text{Re}\mu Ua - \iint_A P_f \frac{dh}{dx} dx dy + C_L \rho\Omega V\omega_y, \quad (1)$$

and,

$$\rho\Omega \left[C_m^{\perp} \frac{dV}{dt} + \frac{1}{2} \left(\frac{dC_m^{\parallel}}{dH} U^2 - \frac{dC_m^{\perp}}{dH} V^2 \right) \right] = \rho g\Omega \cos(\theta) - \frac{\pi}{4} C_D^{\perp} \text{Re}\mu Va - \iint_A P_f dx dy - C_L \rho\Omega U\omega_y, \quad (2)$$

respectively. Here, ρ denotes the air density, Ω denotes the bubble volume, and μ denotes the dynamic viscosity of water. $\text{Re}=2\rho_w V_T a/\mu$ is the Reynolds number with ρ_w denoting the water density and V_T denoting the bubble's terminal rising velocity. C_m , C_D , and C_L denote the coefficients of added mass, drag, and lift, respectively. In addition, the components of coefficients along X and Y are denoted with superscripts \parallel and \perp , respectively. The terms on the left hand side of Eq. (1) and Eq. (2) refer to the inertia terms including the added mass force, while the right-hand side terms correspond to the buoyancy force, the drag force, the thin film force, and the lift force, respectively. More details about the expressions used for each coefficient and how the thin film force is calculated can be found in [11].

The domain is divided into 105×105 nodes. The equations are discretized using a finite difference method and are solved using a MATLAB ode15s solver. We make sure that all forces are continuously computed over the entire simulation time without any discontinuity.

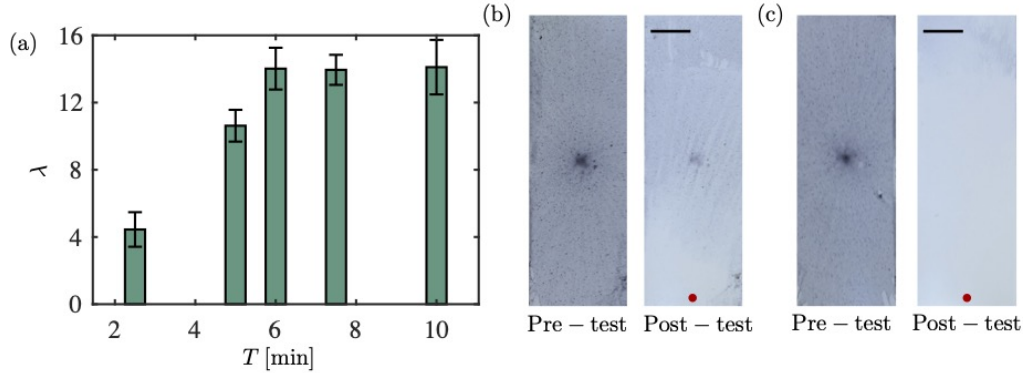


FIG. 4. (a) The cleaning efficacy, λ , for varying test time, T , at $\theta = 20^\circ$. (b) Pre-test and post-test images for $T = 5$ min, and $\theta = 20^\circ$. The scale bar shows 1 cm. (c) Pre-test and post-test images for $T = 6$ min, and $\theta = 20^\circ$. The red dots in post-test images show the location of the bubble releaser. The scale bar shows 1 cm.

Taking into account the size distribution of the bubbles presented in Fig. 2(c), we incorporate $a = 0.6$ mm into our model, as it represents the most frequent bubble size in the experiments. It is assumed that the bubble is at $H = 3$ mm from the surface at $t = 0$ while rising with a measured terminal rising velocity, $V_T \approx 32$ cm/s. We model the bubble motion from $t = 0$ until it reaches the point 6 cm downstream the first impact point along the solid surface. The 6 cm threshold value is chosen to match the average distance traveled by the bubbles in the current experiments. We note that the 6 cm threshold is well beyond the threshold of transitioning from bouncing to sliding regime.

III. RESULTS

We first extract the size distribution for bubbles generated from the 25 gauge needle used at a constant flow rate of $Q = 10$ mL/min in all experiments. Figure 2(a) shows a sample snapshot of bubbles moving along a surface with $\theta = 10^\circ$ from the top view. Figure 2(b) shows surface areas covered by air bubbles over a duration of 0.4 s indicated by using a Gaussian blur at the centers of the bubbles with a root mean square width equal to their radii for the purpose of demonstration. As shown in Fig. 2(b), bubbles adequately cover the slide along the transverse direction. The darker colors near the left end indicate the slower tangential motion of the bubbles along the surface near their impact point. Figure 2(c)

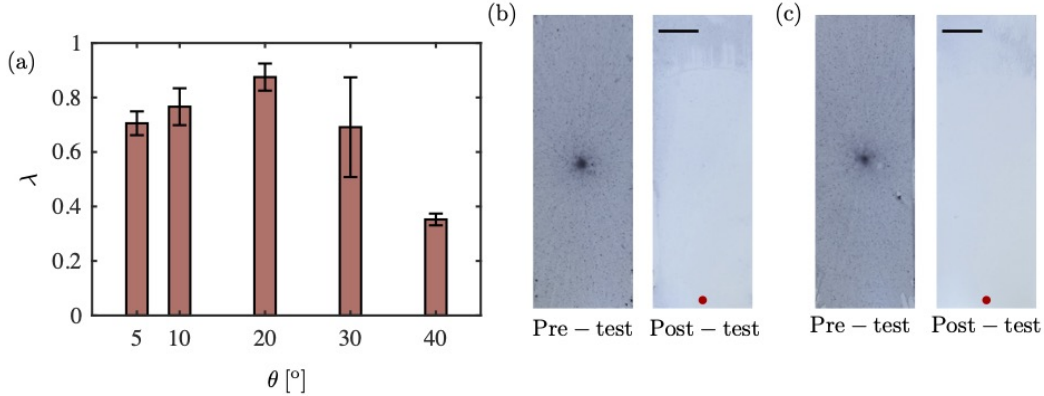


FIG. 5. (a) The efficacy of cleaning, λ , on surfaces coated with proteins for varying surface angles, θ , with $T = 6$ min. (b) Pretest and post-test images for $\theta = 10^\circ$, and $T = 6$ min. The scale bar shows 1 cm. (c) Pre-test and post-test images for $\theta = 20^\circ$, and $T = 6$ min. The red dots in the post-test images show the location of the bubble releaser. The scale bar shows 1 cm.

shows the probability histogram of the extracted bubble radius, a , for five different trials over 200 bubbles. Here, $a = 0.6$ mm is the most frequent average bubble size as the bubble radius in simulations.

We first run a series of protein tests with different cleaning times, T . Figures 4(b) and 4(c) show the pre-test and post-test images at $\theta = 20^\circ$ with two different times: $T = 5$ min and $T = 6$ min, respectively. Figure 4(a) shows λ for $T = 2.5, 5, 6, 7.5,$ and 10 min with $\theta = 20^\circ$. As indicated in Fig. 4(a), λ increases with T until it plateaus out after $T = 6$ min. Therefore, we choose $T = 6$ min as the reference test time on surfaces coated with proteins with different θ . Next, we perform the cleaning experiments at five different angles, $\theta = 5^\circ, 10^\circ, 20^\circ, 30^\circ,$ and 40° for 6 minutes. As shown in Fig. 5(a), the cleaning efficacy, λ , first increases with angle up to $\theta > 20^\circ$, then decreases rapidly. Two representative cases ($\theta = 10^\circ$ and $\theta = 20^\circ$) are shown in Fig. 5(b) and Fig. 5(c), respectively.

In addition, we conduct cleaning experiments with surfaces coated with bacterial biofilm following the procedure described in section II A 3. We note that the biofilm tests are all conducted for 2 minutes to avoid any delamination of the film and catch up the fast removal time. Also, we notice that λ does not increase noticeably for bacteria tests beyond 2 minutes of experiment. Figure 6 (a) shows that the maximum λ occurs at $\theta = 20^\circ$ similarly to the protein tests. Figures 6(b) and 6(c) show the pre-test and post-test images from two cases

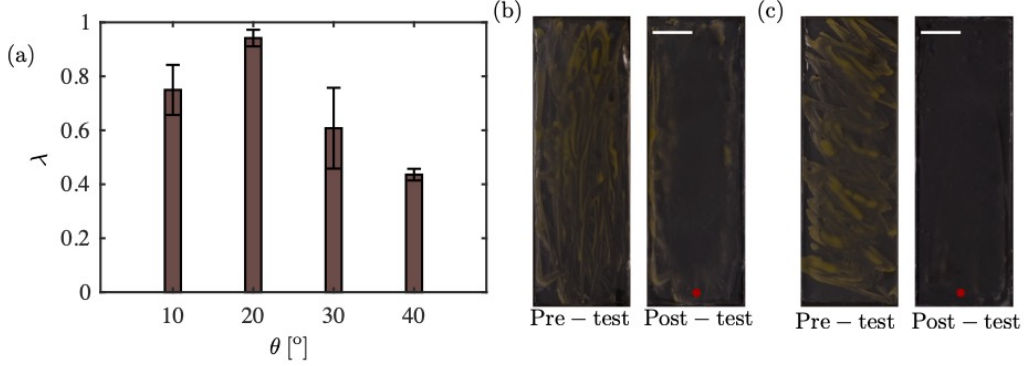


FIG. 6. (a) The cleaning efficacy, λ , on surfaces coated with bacteria for varying surface angles, θ , with $T = 6$ min. (b) Pre-test and post-test images for $\theta = 10^\circ$, and $T = 6$ min. The scale bar shows 1 cm. (c) Pre-test and post-test images for $\theta = 20^\circ$, and $T = 6$ min. The red dots in post-test images show the syringe needle projection on the surface. The scale bar shows 1 cm.

corresponding to $\theta = 10^\circ$ and $\theta = 20^\circ$, respectively.

Next, let us discuss the results obtained from the numerical model that was described in section II C. The average shear force, \overline{F}_s , exerted by the bubble on the surface is the key parameter relevant to cleaning experiments. To characterize \overline{F}_s , we need to discuss two primary factors that affect the shear force of a bubble: the steady film thickness and the steady sliding speed. Figure 7 shows the 3D bubble shape during the steady sliding regime for $a = 0.6$ mm, and $\theta = 20^\circ$. During the steady sliding regime, the bubble shape and the thin film profile do not change noticeably. Figure 7 inset shows the zoom-in view of the 3D bubble shape close to the surface where a dimple forms as previously reported [11, 38, 39]. In addition, Fig. 7 reveals a thinner neck forming on the receding side of the dimple compared to the advancing side. The film thickness on the receding side is of great importance, as the shear force on the surface is mainly composed of the cumulative shear force terms from the mesh points in this thin region.

To gain better insight into the shear force on the surface, we explore the 2D bubble profile in the xz plane for $y = 0$ μm , 100 μm , and 200 μm . Figure 8 indicates the bubble profile for $\theta = 10^\circ$, $\theta = 20^\circ$, and $\theta = 30^\circ$ along different $x - z$ planes. The solid line shows the bubble shape along the central axis, while the dashed line and the dotted dashed line show the profile at $y = 100$ μm and $y = 200$ μm off from the centerline, respectively. The inset plot shows a zoom-in profile near the centerline. Figure 8 shows that the thickness of the film

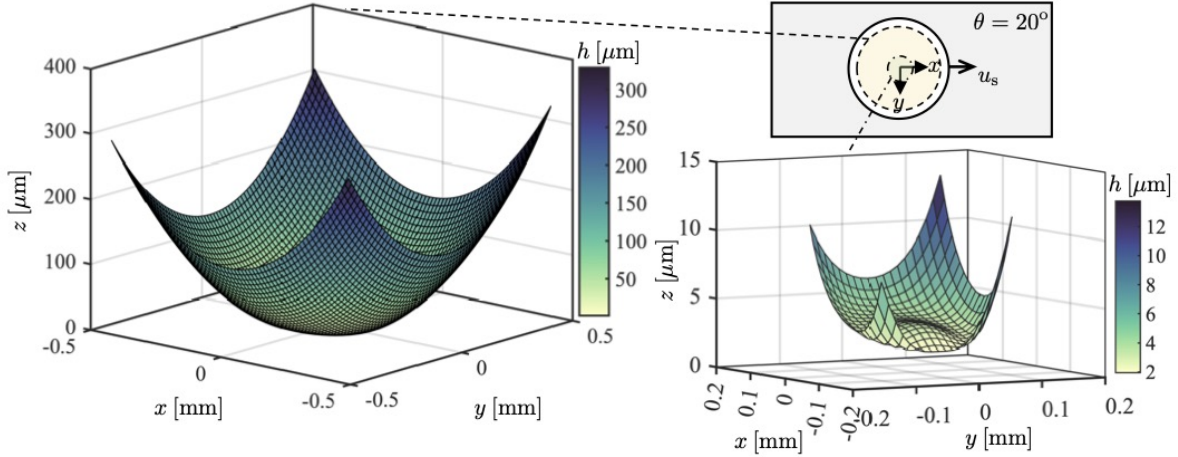


FIG. 7. Bubble profile for $a = 0.6$ mm and $\theta = 20^\circ$ during the steady state sliding. The inset shows the zoom-in view of the dimple formed on the bubble, near the solid surface.

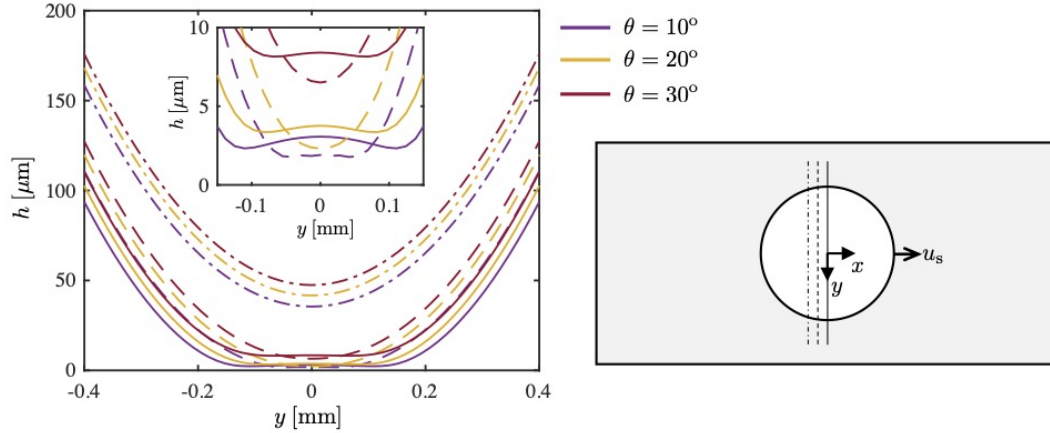


FIG. 8. The bubble profile during the steady state sliding in xz planes at $y = 0$ μm (solid line), $y = \pm 100$ μm (dashed line), and $y = \pm 200$ μm (dotted dashed line) with $a = 0.6$ mm for $\theta = 10^\circ$ (violet), $\theta = 20^\circ$ (yellow), and $\theta = 30^\circ$ (red). The inset shows the zoom in view of the profile near the centerline.

increases with increasing θ . In addition, the dashed lines in Fig. 8 indicate that the dimple size is less than 100 μm from the center along y . Figure 9 shows the bubble 2D profile in the yz plane at $x = 0$ μm , 100 μm , and 200 μm with the tilted angle of $\theta = 10^\circ$, 20° , and 30° . The bubble profile is symmetric about the plane of $y = 0$ as shown in Fig. 9. Additionally, Fig. 9 shows that the dimple width decreases with increasing θ .

Figure 10 shows the steady sliding velocity, u_s , with different angles. As indicated in Fig.

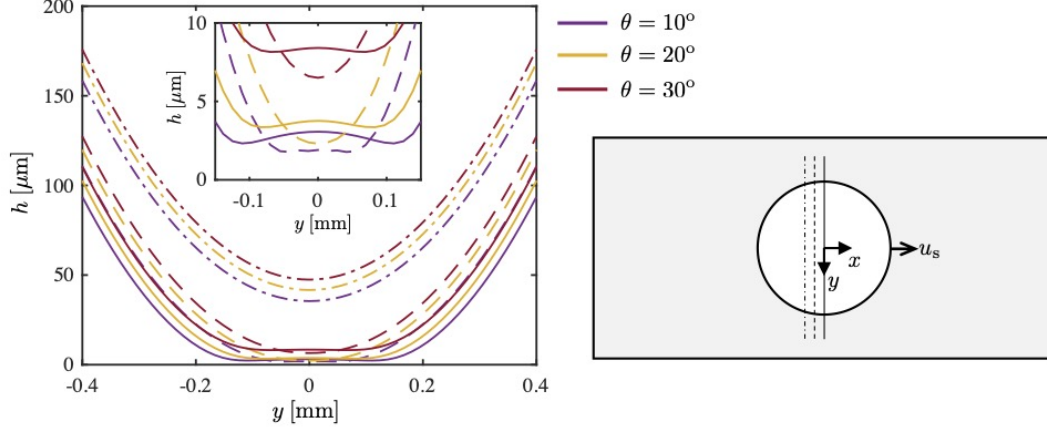


FIG. 9. The bubble profile during the steady state sliding in yz planes at $x = 0 \mu\text{m}$ (solid line), $x = \pm 100 \mu\text{m}$ (dashed line), and $x = \pm 200 \mu\text{m}$ (dotted dashed line) with $a = 0.6 \text{ mm}$ for $\theta = 10^\circ$ (violet), $\theta = 20^\circ$ (yellow) and $\theta = 30^\circ$ (red). The inset shows the zoom-in view of the profile near the centerline.

10, u_s computed from numerical simulations is in good agreement with the experiments. The experimental data presented in Fig. 10 are collected in a separate series of experiments in which single air bubbles with $a = 0.6 \text{ mm}$ and a standard deviation of 0.03 mm are recorded while injected individually. To discuss our results, we consider a bubble sliding along the surface due to the buoyancy force while experiencing an opposing drag force. Along the direction of sliding, the force balance shows $\rho g \Omega \sin \theta \simeq 6\pi\mu a u_s$, which leads to $u_s \simeq (\rho g \Omega / 6\pi\mu a) \sin \theta = (2\rho g a^2 / 9\mu) \sin \theta \approx 0.4 \sin \theta \text{ [m/s]}$ using $\rho = 980 \text{ kg m}^{-3}$, $g = 9.8 \text{ m s}^{-2}$, $a = 6 \times 10^{-4} \text{ m}$, and $\mu \approx 2 \times 10^{-3} \text{ kg m}^{-1} \text{ s}^{-1}$. This relation is slightly off from the best-fit $u_s = 0.25 \sin \theta \text{ [m/s]}$ by a factor of 1.6 only (see Fig. 10).

Next, we consider the force balance along the normal direction to the surface. The normal force in the lubrication approximation becomes $\mu u_s (A/h) / \sin \theta$, which balances with the normal buoyancy force $\rho g \Omega \cos \theta$. Under the assumption that the contact area, A , is proportional to a^2 , $h \simeq \frac{\mu A}{\rho g \Omega} \frac{\rho g \Omega}{6\pi\mu a} (\cos \theta)^{-1} = \frac{A}{6\pi a} (\cos \theta)^{-1}$. Here, A is the area where the shear force is dominant. We assume that A is the circular domain of radius $= 0.2a$ corresponding to the dimple size. Then, the film thickness becomes $h \simeq 2(\cos \theta)^{-1} \mu\text{m}$, which shows about $2 \mu\text{m}$ at $\theta = 0$ close to what we found in the simulation in Figs. 8 and 9. In terms of the θ -dependence, Fig. 11 shows that h is proportional to $(\cos 2\theta)^{-1}$ not $(\cos \theta)^{-1}$. This is presumably due to the complicated interplay between various forces: buoyancy, drag, and

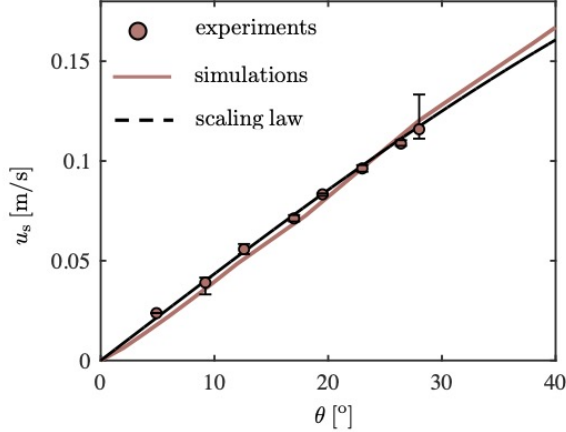


FIG. 10. Comparison of the steady-state sliding velocity, u_s for varying θ between the experiments (symbols), the simulations (solid line), and the scaling laws (dashed line). The dashed line shows $u_s = 0.25 \sin \theta$. The errorbars represent 3 trials.

thin film force, which cannot not be captured in this simple scaling argument.

Finally, we compute the mean shear force on the surface along X as $\overline{F}_s = \int_0^{6 \text{ cm}} F_s dX$ where F_s denotes the temporal shear force on the surface. We note that \overline{F}_s beyond 6 cm does not change significantly. Hence, the resulting average value is close to the steady-state value. However, decreasing the integration domain to a length scale comparable to the length of the bouncing regime may lead to a different result which is out of the scope of the current study. Following the simple analytical expressions $u_s \propto \sin \theta$ and $h \propto (\cos 2\theta)^{-1}$, the shear stress scales as $\overline{F}_s \approx \mu u_s A / h = 0.25 \mu \sin \theta (6\pi a) \cos(2\theta) \approx 3\pi \cdot 0.6 \times 10^{-6} \sin \theta \cos(2\theta) \text{ [N]} = 5.65 \sin \theta \cos(2\theta) \text{ [\mu N]}$. We then find the roots for the derivative of $\sin \theta \cos(2\theta)$ using Newton's method which gives $\theta_{\text{cr}} \approx 24^\circ$ close to the values seen in both experiments and simulations. In addition, since we are in a small slope regime, we can simply add a unity or $\cos \theta$ to the expression for \overline{F}_s . Then, the shear stress becomes $\overline{F}_s \sim 5.65 \sin \theta \cos \theta \cos(2\theta) \text{ [\mu N]} \simeq 2.82 \sin(2\theta) \cos(2\theta) \text{ [\mu N]} = 1.41 \sin(4\theta) \text{ [\mu N]}$. Therefore, the shear stress is maximized around $\theta \simeq \pi/8$ (i.e., $4\theta = \pi/2$), which is very close to what we observed in both simulations and experiments. It is worth noting that the magnitude of the stress computed in the simulations is a bit higher than the value we predict from the simple theory. This is presumably because our analytical theory estimates the shear stress on a circular dimple and not on the entire bubble.

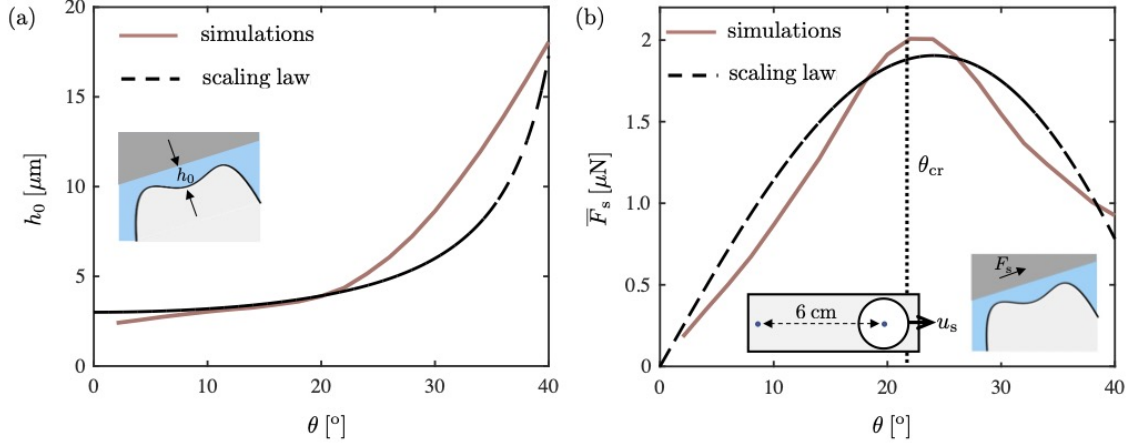


FIG. 11. (a) Simulation (solid line), and scaling law (dashed line) results for the steady film thickness in the center of the bubble, h_0 , at varying θ . The dashed line shows $h_0/\cos(2\theta)$ with $h_0 = 3 \mu\text{m}$. (b) Simulation (solid line), and scaling law (dashed line) results for the shear force, \bar{F}_s , over the surface averaged from $X = 0 - 6 \text{ cm}$ at varying θ . The dashed line shows $\bar{F}_s = 7 \times 10^{-6} \sin \theta \cos(2\theta)$.

IV. DISCUSSIONS

We examined the cleaning effect of millimetric bubbles at different inclination angles of the substrate coated with either proteins or bacterial biofilm. Our results indicated that both coatings produce similar cleaning results, where $\theta \simeq 22^\circ \simeq \pi/8$ gives the highest cleaning parameter, λ . This consistent result with both protein coating and bacterial coating suggests that surface wettability is not a key factor in cleaning, but that the angle of inclination is. We also computationally investigated the bubble impact at different surface angles from the first impact moment until the bubble reaches the edge of the surface in a steady sliding regime. Our numerical model indicated that while the steady sliding speed increases with the inclination angle, the characteristic film thickness between the bubble and the surface also increases. Since the sliding speed and the film thickness have counter effects on the shear force, their interaction yields the maxima in shear force vs. surface angle.

The current study investigates the role of surface geometry (i.e., inclination angle) in the use of air bubbles as a sustainable method to effectively sanitize surfaces contaminated with active or passive coatings. This method can be advantageous in cleaning surfaces of soft materials such as fruits and vegetables, where conventional methods damage the soft tissues

of the produce. In addition, our findings on the optimal cleaning angle can be leveraged to design bubble-cleaning machinery applicable to biomedical devices. Further studies are required to fully characterize the role of bubble size on the most effective angle to account for polydisperse bubble injection. In addition, studying bubble dynamics on curved surfaces is a relevant topic that will be addressed in the future study.

ACKNOWLEDGMENTS

This work was supported by the National Science Foundation (NSF) under Grant No. CBET-1919753.

-
- [1] S. B. G. O'Brien and B. H. A. A Van Den Brule, "A mathematical model for the cleansing of silicon substrates by fluid immersion," *Journal of Colloid and Interface Science* **144**, 210–221 (1991).
 - [2] C. Gómez-Suárez, J. Noordmans, H. C. van der Mei, H. J. Busscher, "Removal of Colloidal Particles from Quartz Collector Surfaces As Stimulated by the Passage of Liquid-Air Interfaces," *Langmuir* **15**, 5123-5127 (1999).
 - [3] S. Khodaparast, M. K. Kim, J. E. Silpe, H. A. Stone, "Bubble-Driven Detachment of Bacteria from Confined Microgeometries," *Environmental Science & Technology* (2017).
 - [4] P. R. Gogate, A. B. Pandit, "A review of imperative technologies for wastewater treatment I: oxidation technologies at ambient conditions," *Advances in Environmental Research* **8**, 501-551 (2004).
 - [5] Y. J. Chan, M. F. Chong, C. L. Law, D. G. Hassell, "A review on anaerobic-aerobic treatment of industrial and municipal wastewater," *Chemical Engineering Journal* **155**, 1-18 (2009).
 - [6] T. Temesgen, T. T. Bui, M. Han, T. Kim, H. Park, "Micro and nanobubble technologies as a new horizon for water-treatment techniques: A review," *Advances in Colloid and Interface Science* (2017).
 - [7] M. Menesses, J. Belden, N. Dickenson, J. and Bird, "Measuring a critical stress for continuous prevention of marine biofouling accumulation with aeration," *Biofouling*, 1-9 (2017).

- [8] G. A. Hopkins, F. Gilbertson, O. Floerl, P. Casanovas, M. Pine, P. Cahill, "Continuous bubble streams for controlling marine biofouling on static artificial structures," *PeerJ* **9** (2021).
- [9] S. Jung, J. Eifert, "Cleaning fruits using micro-bubbles," (2016).
- [10] J. J. Lee, J. D. Eifert, S. Jung, L. K. Strawn, "Cavitation Bubbles Remove and Inactivate *Listeria* and *Salmonella* on the Surface of Fresh Roma Tomatoes and Cantaloupes," *Frontiers in Sustainable Food Systems* **2**, 61 (2018).
- [11] E. Esmaili, P. Shukla, J. D. Eifert, S. Jung, "Bubble impact on a tilted wall: Removing bacteria using bubbles," *Phys. Rev. Fluids* **4**, 043603 (2019).
- [12] E. Scallan, R. M. Hoekstra, F. J. Angulo, R. V. Tauxe, M. Widdowson, S. L. Roy, J. L. Jones, P. M. Griffin, "Foodborne illness acquired in the United States—major pathogens," *Emerging infectious diseases* **17**, 7 (2011).
- [13] E. Scallan, P. M. Griffin, F. J. Angulo, R. V. Tauxe, R. M. Hoekstra, "Foodborne illness acquired in the United States—unspecified agents," *Emerging infectious diseases* **17**, 16 (2011).
- [14] J. G. Morris Jr., "How safe is our food?," *Emerging infectious diseases* **17**, 126 (2011).
- [15] R. Clift, J. R. Grace, M. E. Weber, Bubbles, drops, and particles, (Courier Corporation, 2005).
- [16] P. C. Duineveld, "The rise velocity and shape of bubbles in pure water at high Reynolds number," *Journal of Fluid Mechanics* **292**, 325-332 (1995).
- [17] L. Amaya-Bower, T. Lee, "Single bubble rising dynamics for moderate Reynolds number using lattice Boltzmann method," *Computers & Fluids* **39**, 7 (2010).
- [18] F. Peters, C. Els, "An experimental study on slow and fast bubbles in tap water," *Chemical engineering science* **82**, 194-199 (2012).
- [19] M. Wu, M. Gharib, "Experimental studies on the shape and path of small air bubbles rising in clean water," *Physics of Fluids* **14**, L49–L52 (2002).
- [20] R. Manica, E. Klaseboer, D. Y. C. Chan, "Force balance model for bubble rise, impact, and bounce from solid surfaces," *Langmuir* **31**, 6763-6772 (2015).
- [21] J. Zawala, "“Immortal” liquid film formed by colliding bubble at oscillating solid substrates," *Physics of Fluids* **28**, 057103 (2016).
- [22] J. Zawala, D. Kosior, T. Dabros, K. Malysa, "Influence of bubble surface fluidity on collision kinetics and attachment to hydrophobic solids," *Colloids and Surfaces A: Physicochemical and Engineering Aspects* **505**, 47-55 (2016).

- [23] M. Krasowska, K. Malysa, "Kinetics of bubble collision and attachment to hydrophobic solids: I. Effect of surface roughness," *International Journal of Mineral Processing* **81**, 205-216 (2007).
- [24] R. Zenit, D. Legendre, "The coefficient of restitution for air bubbles colliding against solid walls in viscous liquids," *Physics of Fluids* **21**, 083306 (2009).
- [25] E. Klaseboer, R. Manica, M. H. W. Hendrix, C. Ohl, D. Y. C. Chan, "A force balance model for the motion, impact, and bounce of bubbles," *Physics of Fluids* **26**, 092101 (2014).
- [26] A. W. G. de Vries, A. Biesheuvel, L. van Wijngaarden, "Notes on the path and wake of a gas bubble rising in pure water," *International Journal of Multiphase Flow* **28**, 1823-1835 (2002).
- [27] F. Takemura, J. Magnaudet, "The transverse force on clean and contaminated bubbles rising near a vertical wall at moderate Reynolds number," *Journal of Fluid Mechanics* **495**, 235-253 (2003).
- [28] M. F. Moctezuma, R. Lima-Ochoterena, R. Zenit, "Velocity fluctuations resulting from the interaction of a bubble with a vertical wall," *Physics of Fluids* **17**, 098106 (2005).
- [29] B. Figueroa-Espinoza, R. Zenit, D. Legendre, "The effect of confinement on the motion of a single clean bubble," *Journal of Fluid Mechanics* **616**, 419-443 (2008).
- [30] T. Maxworthy, "Bubble rise under an inclined plate," *Journal of Fluid Mechanics* **229**, 659-674 (1991).
- [31] H. Tsao, D. L. Koch, "Observations of high Reynolds number bubbles interacting with a rigid wall," *Physics of Fluids* **9**, 44-56 (1997).
- [32] A. Perron, L. I. Kiss, S. Poncsak, "An experimental investigation of the motion of single bubbles under a slightly inclined surface," *International Journal of Multiphase Flow* **32**, 606-622 (2006).
- [33] B. Podvin, S. Khoja, F. Moraga, D. Attinger, "Model and experimental visualizations of the interaction of a bubble with an inclined wall," *Chemical Engineering Science* **63**, 1914-1928 (2008).
- [34] C. E. Norman, M. J. Miksis, "Dynamics of a gas bubble rising in an inclined channel at finite Reynolds number," *Physics of Fluids* **17**, 022102 (2005).
- [35] K. M DeBisschop, M. J. Miksis, D. M. Eckmann, "Bubble rising in an inclined channel," *Physics of Fluids* **14**, 93-106 (2002).

- [36] C. Barbosa, D. Legendre, R. Zenit, "Sliding motion of a bubble against an inclined wall from moderate to high bubble Reynolds number," *Physical Review Fluids* **4**, 043602 (2019).
- [37] A. Hooshanginejad, T. Sheppard, J. Manyallah, J. Jaicks, S. Jung, "Cleaning effect of bubbles impacting tilted walls under acoustic waves," *Proceedings of the ASME FEDSM*, FEDSM2022-86897 (2022).
- [38] D. Platikanov, "Experimental investigation on the "dimpling" of thin liquid films," *The Journal of Physical Chemistry* **68**, 3619-3624 (1964).
- [39] L. Pan, S. Jung, R. Yoon, "Effect of hydrophobicity on the stability of the wetting films of water formed on gold surfaces," *Journal of colloid and interface science* **361**, 321-330 (2011).